Effect of crystal orientation on ruby R-line shifts under shock compression and tension

X. A. Shen* and Y. M. Gupta
Shock Dynamics Laboratory, Department of Physics, Washington State University, Pullman, Washington 99164-2814
(Received 28 December 1992)

We have examined the effect of crystal orientation on ruby R-line shifts under shock compression and tension by measuring shifts in crystals shocked along the ruby a axis and comparing these with the earlier shock data along the c axis and hydrostatic measurements. Additionally, we have extended the theoretical work of Sharma and Gupta [Phys. Rev. B **43**, 879 (1991)] on strain-induced shifts of the ruby R lines to permit analysis of R-line shifts for arbitrary deformation. The experimental results show strong anisotropy in R-line shifts for both compression and tension and provide direct evidence of site-symmetry changes under shock loading. The nonlinear increase in R_1-R_2 splitting for both compression and tension along the a axis is in marked contrast to the c-axis data. Unlike the spectroscopy results, the continuum response of sapphire (or ruby) is isotropic. The theoretical developments permit consistent analyses of all available shock, hydrostatic, and uniaxial-stress-deformation data on R-line shifts.

I. INTRODUCTION

The wavelength shift of the ruby (Al_2O_3:Cr^{3+}) R lines is commonly used for pressure calibration in diamond-anvil-cell (DAC) measurements.[1-5] At very high pressures in DAC studies, the stress state is nonhydrostatic and a good understanding of the R-line shifts under nonhydrostatic loading is desirable.[6] Toward this end, we have developed methods in our laboratory to examine the R-line shifts under shock-wave uniaxial-strain loading.[7,8] In an earlier study,[9] the R-line shifts of ruby shocked along the crystal c axis have been examined and compared with hydrostatic data. The c-axis results showed clearly the effects of nonhydrostaticity on both line shifts and R-line separation. Subsequently, experimental methods were developed to examine R-line shifts in crystals subjected to uniaxial tensile strain, along the c axis, to tensile stresses as high as 108 kbar.[10]

Apart from the ruby calibration issue, the results from shock-wave experiments along the c axis suggest the possibility of using the optical spectra as a microscopic probe of shock-induced changes in crystalline solids. The ruby R lines, because of their sharpness and sensitivity to deformation, are well suited for this purpose. The recent theoretical work by Sharma and Gupta[11] to analyze the R-line shifts under different deformation conditions was motivated in large part by this possibility. The developments in Ref. 11, using some of the present data, describe a theoretical method to analyze a wide variety of experimental measurements in a consistent manner and to relate site-symmetry changes around the Cr^{3+} ion to macroscopic deformation. The present work is a part of a comprehensive effort to understand the response of ruby R-line shifts under well-characterized loading conditions.

In this paper we present experimental results describing ruby R-line shifts for crystals shocked along the crystal a axis. Both compression (to 125 kbar) and tension (to 105 kbar) data are presented and compared with corresponding c-axis data. The intent of this work was to understand the effect of crystal orientation on the ruby R-line shifts under well-defined nonhydrostatic loading. Unlike static measurements, the samples in shock experiments are subjected to strongly nonhydrostatic but uniform loading. Hence these data can be used to separate contributions of nonhydrostaticity, orientation, and nonuniform compression to R-line shifts. The part of our work that pertains to pressure calibration in DAC measurements has been published elsewhere[12] and will not be discussed here.

The present work had the following main objectives: (a) to develop a detailed understanding of the R-line shifts caused by elastic deformations along different crystal axes as a prelude for relating the effects of inelastic deformation to R-line shifts, (b) to compare continuum and optical response of shocked ruby to relate macroscopic and microscopic deformations in shocked sapphire, and (c) to provide data for the development of a crystal-field model for analyzing R-line shifts under different deformation conditions. In the present paper, we also present theoretical developments that extend the analytic work of Sharma and Gupta[11] and permit analysis of arbitrary deformations in shocked ruby crystals.

Because the theoretical developments in this paper are based on the work in Ref. 11, a number of minor errors in Ref. 11 are summarized in an erratum that appears in this issue.

II. THEORETICAL DEVELOPMENTS

A phenomenological model, based on symmetry-adapted strains in conjunction with crystal-field theory, was developed recently to describe stress-induced shifts of the ruby R lines.[11] Using this model, the observed R-line shifts under different deformation conditions, including shock-wave deformation, hydrostatic compression, and quasistatic uniaxial-stress compression along the c and a axes, have been analyzed consistently. Although good agreement between theoretical predictions and mea-

surements was obtained, some of the analysis in Ref. 11 was restricted to very small strain values. Also, the earlier analysis was restricted to deformations along the c and a axes.

In this section we first summarize the work of Sharma and Gupta, along with some of their important findings relevant to the present work. Next, we describe modifications to their theoretical work that make the results more general and make it easier to analyze experimental data for a broad range of loading conditions. We emphasize that all of the model parameters, as before,[11] were obtained directly from shock-wave compression results along the c and a axes.

In ruby, the R-line luminescence originates from the transition of localized d electrons of the Cr^{3+} impurity ion.[13] The Cr^{3+} ion is surrounded by six nearest-neighbor O^{2-} ions, forming almost an octahedron. Transition energy of the d electrons in the Cr^{3+} ion, associated with R-line luminescence, is determined mainly by these six nearest-neighbor O^{2-} ions.[13] The Hamiltonian describing the localized electron states of the Cr^{3+} ion can be written as[11]

$$H_{\text{total}}=H_{\text{oct}}+H_{\text{trig}}+H_{\text{s.o.}}+H_{\text{strain}} , \tag{1}$$

where H_{oct} includes all interactions with octahedral or higher symmetry, H_{trig} represents interactions that have trigonal symmetry, $H_{\text{s.o.}}$ denotes the spin-orbit interaction, and H_{strain} represents the strain-induced change in the total Hamiltonian. In the calculations in Ref. 11, the unperturbed Hamiltonian describing the idealized first-neighbor interaction has octahedral symmetry; the last three terms in Eq. (1) were treated as perturbations with respect to H_{oct}. In an octahedral system, an arbitrary strain around the Cr^{3+} ion can be expressed in terms of the irreducible strain representations of the octahedral group, i.e., $H_{\text{strain}}=H_{A_1}+H_E+H_{T_2}$, where A_1, E, and T_2 denote the three irreducible representations.[11] As before, strains are assumed positive in compression.

The ruby R-line shifts were analyzed in terms of the mean shift of the R_1 and R_2 lines and the change in R_1-R_2 separation by Sharma and Gupta.[11] They introduced four parameters to describe the shifts of the R lines: $\Pi(A_1)$, $\Pi(e_{x_0})$, Δ, and Q. In their work, $\Pi(A_1)$ characterizes the mean of the R_1 and R_2 shifts due to the uniform strain $e(A_1)$. $\Pi(e_{x_0})$ characterizes the linear contribution of trigonal strain e_{x_0} to the mean shift. Δ describes the R_1-R_2 splitting associated with the trigonal strain e_{x_0}. Q describes the splitting changes associated with $e(E)$-type strains. The values of $\Pi(A_1)$ and $\Pi(e_{x_0})$ were determined from shock-wave results to be -1977.5 cm^{-1}/density compression and 645.6 cm^{-1} trigonal strain, respectively. The negative sign denotes a redshift. In the subsequent discussion, the symbol Δ will be used differently than used in Ref. 11. The parameter describing the trigonal-field contribution to R_1-R_2 splitting will be denoted as K in the present work.

The earlier analysis of R_1-R_2 splitting was determined from uniaxial-strain compression along the ruby c and a axes. The eigenmatrices presented in the analysis of Sharma and Gupta,[11] which describe the deformation-induced splitting of the R lines, are valid only for shock deformation along the c and a axes; a general solution for arbitrary loading conditions was not obtained at that time. Furthermore, in deriving the line-splitting expression from their 4×4 eigenmatrix, for compression along the a axis, Sharma and Gupta employed an approximation assuming a small contribution from tetragonal strains.[11] Thus the corresponding parameter, i.e., Q/e_{u_-} [see Eq. (6c) below] that determines the R_1-R_2 splitting for a-axis deformation was valid only for very small deformations.

Here we extend the analysis in Ref. 11 to arbitrary deformations and loading directions, and present an analytical solution for the R_1-R_2 separation by diagonalizing a generalized 4×4 matrix. This approach requires reevaluating all the matrix elements in terms of arbitrary strains. Our calculations summarized in the following paragraphs assume familiarity with the theoretical developments in Ref. 11.

According to the analysis in Ref. 11, the R_1-R_2 splitting can be obtained by diagonalizing an eigenmatrix whose elements are given as[13]

$$\sum_{M_s'',M''}\frac{\langle t_2^3\,{}^2EM_s'M'|H_{\text{pert}}|t_2^3\,{}^2T_2M_s''M''\rangle\langle t_2^3\,{}^2T_2M_s''M''|H_{\text{pert}}|t_2^3\,{}^2EM_sM\rangle}{\varepsilon({}^2E)-\varepsilon({}^2T_2)} , \tag{2}$$

where $t_2^3\,{}^2E$ represents the ${}^2E$ state arising from three electrons in t_{2g}-type states, M_s represents the magnetic quantum number, and M denotes the basis of ${}^2E$ as u_+ and u_- and of ${}^2T_2$ as x_+, x_-, and x_0. This matrix describes the effect of the perturbation terms [i.e., the last three terms in Eq. (1)] on the energy of $t_2^3\,{}^2E$ states which are responsible for the R-line emission. The elements of this eigenmatrix can be evaluated using the Wigner-Eckart theorem (see Chap. 8 of Ref. 13)

$$\langle\alpha\Gamma\gamma|X_{\gamma''}(\Gamma'')|\alpha'\Gamma'\gamma'\rangle = \Gamma^{-1/2}\langle\Gamma\gamma|\Gamma'\gamma'\Gamma''\gamma''\rangle\langle\alpha\Gamma\|X(\Gamma'')\|\alpha'\Gamma'\rangle , \tag{3}$$

where $\langle\Gamma\gamma|\Gamma'\gamma'\Gamma''\gamma''\rangle$ represents the Clebsch-Gordon coefficients. The matrix reduces to a 4×4 matrix since there exist two M_s states $(\frac{1}{2},-\frac{1}{2})$ for each $u_\pm$.

An important aspect of the present work is the recognition that for an arbitrary deformation, the perturbative Hamiltonian due to deformation can be written as

$$\begin{aligned}H_{\text{pert}}&=V_{x_0}^0(T_{2g})+V_{x_0}(T_{2g})+V_{x_+}(T_{2g})\\&\quad+V_{x_-}(T_{2g})+V_{u_+}(E)+V_{u_-}(E)\\&=V_{x_0}^0+(e_{x_0}+e_{x_+}+e_{x_-})V_{T_{2g}}+(e_{u_+}+e_{u_-})V_E ,\end{aligned} \tag{4}$$

where $V^0_{x_0}(T_{2g})$ is the ambient trigonal field, $V_{T_{2g}}$ and V_E are two parameters proportional to the magnitude of trigonal and tetragonal distortions, e_{x_+} and e_{x_-} are rhombic strains, and e_{u_+} and e_{u_-} are tetragonal strains. These irreducible strains are defined with respect to the trigonal axes as indicated in Table II of Ref. 11. As before,[11] we neglect changes in the spin-orbit interaction and the contribution from the A_1 type of strain has been left out in writing Eq. (4); in the actual calculations, the A_1 contributions are included.

Thus the generalized eigenmatrix for arbitrary deformation [that replaces Eq. (19) and (23) in Ref. 11] can be obtained by reevaluating Eq. (2) with H_{pert} given in Eq. (4) as

$$
\begin{array}{c|cccc}
 & u_+,\frac{1}{2} & u_+,-\frac{1}{2} & u_-,\frac{1}{2} & u_-,-\frac{1}{2} \\
u_+,\frac{1}{2} & \frac{M+2K\zeta}{A} & \frac{2\sqrt{2}K_1\zeta e^*_{x_-}}{A} & \frac{N}{A}+qe_{u_-} & 0 \\
u_+,-\frac{1}{2} & \frac{2\sqrt{2}K_1\zeta e_{x_-}}{A} & \frac{M-2K\zeta}{A} & 0 & \frac{N}{A}+qe_{u_-} \\
u_-,\frac{1}{2} & \frac{N^*}{A}+qe^*_{u_-} & 0 & \frac{M-2k\zeta}{A} & -\frac{2\sqrt{2}K_1\zeta e^*_{x_-}}{A} \\
u_-,-\frac{1}{2} & 0 & \frac{N^*}{A}+qe^*_{u_-} & -\frac{2\sqrt{2}K_1\zeta e_{x_-}}{A} & \frac{M+2K\zeta}{A}
\end{array}
, \tag{5}
$$

where $A=\varepsilon(^2E)-\varepsilon(^2T_2)=-6734\ \text{cm}^{-1}$,

$$\zeta=-2\langle t_{2g}\tfrac{1}{2},x_+|H_{\text{s.o.}}|t_{2g}\tfrac{1}{2},x_+\rangle=187\ \text{cm}^{-1}\ , \tag{6a}$$

$$K=K_0+K_1e_{x_0}\ , \tag{6b}$$

$$q=\frac{Q}{e_{u_-}}=\frac{1}{\sqrt{2}}\langle {}^2E\|V_E\|{}^2E\rangle\ , \tag{6c}$$

$$M=6K^2+12K_1^2|e_{x_-}|^2\ , \tag{6d}$$

and

$$N=-12K_1Ke_{x_-}-6K_1^2(e^*_{x_-})^2\ , \tag{6e}$$

with

$$K_0=-\frac{1}{6}\langle t_2^3\,{}^2E\|V^0(T_{2g})\|t_2^3\,{}^2T_2\rangle\ , \tag{6f}$$

$$K_1=-\tfrac{1}{6}\langle t_2^3\,{}^2E\|V_{T_{2g}}\|t_2^3\,{}^2T_2\rangle\ , \tag{6g}$$

and

$$Q=\langle {}^2Eu_+|V_{u_+}(E)+V_{u_-}(E)|{}^2Eu_-\rangle\ . \tag{6h}$$

We point out that the procedure used in obtaining the general expression [Eq. (5)] above is identical to that used in Ref. 11 and that the eigenmatrices for uniaxial-strain loading along the ruby c and a axes derived in Ref. 11 can be deduced easily from Eq. (5) by using the appropriate expressions for the irreducible strains.

In comparing the present results to the expressions in Ref. 11, the following comments are helpful. Here the matrix elements are expressed in terms of general strains rather than those for a specific loading condition as was done before. The trigonal field v in Ref. 11 is now given by Eq. (6b), and it can be shown that $v=-3$ K. Furthermore, the tetragonal distortion is represented here by qe_{u_-} instead of Q.

The matrix in Eq. (5) has the form

$$\begin{pmatrix} A & C & D & 0 \\ C^* & B & 0 & D \\ D^* & 0 & B & -C \\ 0 & D^* & -C^* & A \end{pmatrix} \tag{7}$$

and can be solved analytically for the eigenvalues. However, there exist only two distinct eigenvalues

$$\varepsilon_\pm=\frac{(A+B)\pm[(A-B)^2+4(|C|^2+|D|^2)]^{1/2}}{2}\ . \tag{8}$$

This expression turns out to be identical to the one derived in Ref. 11. However, in obtaining it, Sharma and Gupta used an incorrect matrix [see Eq. (A1) in Ref. 11] along with an assumption of small D, which is not valid in general.

The R_1-R_2 splitting can be obtained from these two eigenvalues as

$$\Delta=(\varepsilon_+-\varepsilon_-)$$
$$=\left[\left[\frac{4K\zeta}{A}\right]^2+2\left[\frac{4K_1\zeta}{A}\right]^2|e_{x_-}|^2+4\left|qe_{u_-}+\frac{12K_1Ke_{x_-}+6K_1^2(e^*_{x_-})^2}{A}\right|^2\right]^{1/2}\ . \tag{9}$$

We emphasize that this expression for R_1-R_2 splitting is valid for arbitrary deformations or loading directions as long as an octahedral basis can be used to represent the unperturbed Hamiltonian. The relationship between the usual strain tensor and the irreducible strain components

used here has been tabulated in Table II of Ref. 11. By evaluating the irreducible strain components for a given deformation, Eq. (9) can be evaluated.

For uniaxial strain e along the c axis, the only nonvanishing irreducible strains are[11] $e(A_1)=e$ and $e_{x_0}=e/\sqrt{3}$. Therefore the change in splitting becomes

$$\Delta-\Delta_0=-\frac{4K_1\zeta}{A}e_{x_0}\ , \tag{10}$$

where K_1 is a constant to be determined from the experiment.

For uniaxial strain along the a axis, all six irreducible strain components exist:[11]

$$e(A_1)=e\ , \tag{11a}$$

$$e_{x_0}(T_2)=-\frac{e}{2\sqrt{3}}\ , \tag{11b}$$

$$e_{x_+}(T_2)=-e^*_{x_-}(T_2)=\frac{(1-i\sqrt{3})}{4}\frac{e}{\sqrt{3}}\ , \tag{11c}$$

and

$$e_{u_+}(E)=-e^*_{u_-}(E)=\frac{(1-i\sqrt{3})}{2\sqrt{2}}\frac{e}{\sqrt{3}}\ . \tag{11d}$$

The R_1-R_2 separation for a-axis deformation becomes

$$\Delta=4\left\{\left[\frac{K\zeta}{A}\right]^2+\frac{1}{6}\left[\frac{K_1\zeta e}{A}\right]^2+\left[\left[\frac{\sqrt{3}K_1K}{A}+\frac{q}{2\sqrt{6}}\right]e+\frac{K_1^2e^2}{4A}\right]^2\right\}^{1/2}\ . \tag{12}$$

Here the only unknown parameter besides K_1 is q. Equation (12) differs slightly from Eq. (38a) presented in Ref. 11, where a term corresponding to $K_1^2e^2/4A$ was neglected; in comparing Eq. (12) to Eq. (38a) in Ref. 11, recall that $\Delta v=-3K_1e_{x_0}$. In Sec. V, we will discuss the effect of the K_1^2 term on the overall change of R_1-R_2 splitting for a-axis deformation.

Equations (10) and (12) show that the parameters K_1 and q can be determined separately from shock-wave measurements along the crystal c and a axes. The R_1-R_2 separation measured earlier along the crystal c axis [Eq. (4) in Ref. 11] suggests the value of K_1 to be approximately -3459.5 cm^{-1}/trigonal strain. We postpone the evaluation of q until we discuss the R_1-R_2 splitting for shock compression along the a axis in Sec. V C.

The above modification to the work of Sharma and Gupta provides an exact solution for the R-line splitting within the general theoretical framework described in their paper; no approximation was made in deriving Eq. (9). Thus strain-induced changes in R_1-R_2 splitting can now be calculated for arbitrary deformation. In the subsequent discussion, however, we will concentrate primarily on uniaxial-strain deformation along the ruby c and a axes, i.e., Eqs. (10) and (12), because the shock-wave results discussed here were obtained for these two orientations. In the remainder of this section, we comment briefly on deformations that were explicitly examined in Ref. 11 but are not discussed in detail in this paper.

In view of the present modifications, we also comment on the analysis of uniaxial-stress results in Ref. 11. In the earlier analysis, the line splitting for uniaxial-stress compression along the a axis was calculated using the expression for uniaxial-strain loading, [Eq. (38a) in Ref. 11]; this approach is not correct. However, because the compression discussed was modest, the use of the present analysis does not result in significant changes and the earlier conclusions are still valid.

Another important parameter which describes the quadratic contribution of strains to the mean shift of the R_1 and R_2 lines also needs to be discussed here in order to analyze the observed curvature of the R_2 line in tension (Sec. V B). This parameter can be readily obtained from Eq. (6d), which is proportional to the mean shift.[11] This equation shows that the quadratic term for the mean, i.e., $6K_1^2e_{x_0}^2+12K_1^2|e_{x_-}|^2$, is determined only by trigonal and rhombic strains. Tetragonal strains, however, have no effect on the mean shift of the R lines and contribute to only the R_1-R_2 separation as shown in Eq. (9). For shock compression along the c axis, only the trigonal strain exists (since $e_{x_-}=0$), while for shock deformation along the a axis both trigonal and rhombic strains contribute to the curvature. Thus the curvature ratio for shock compression along the a and c axes can be evaluated using appropriate expressions for the trigonal and rhombic strains for the two axes.[14]

The curvature ratio for shock compression along the c and a axes has also been discussed in Ref. 11. However, the earlier discussion pertained only to these two particular orientations and the general solution for the curvature of the mean shift was not obtained. Furthermore, the curvature of the mean shift in Ref. 11 was discussed in terms of mean stresses rather than strains. This approach is not as useful in general because strain and mean stress are often not linearly related.

A detailed discussion of hydrostatic effects has been presented in Ref. 11. Under hydrostatic-stress conditions, the only nonvanishing strain components are $e(A_1)$ and $e_{x_0}(T_2)$. Further analysis shows that the magnitude of the trigonal strain is extremely small [e.g., 0.000 78 at 100 kbar (Ref. 11)] and its contribution to mean shift and splitting can be ignored. Thus the overall shift of the R lines is determined only by uniform strain.

III. EXPERIMENTAL METHOD

The experimental techniques used in the present work are similar to those used in earlier studies.[8–10] Hence only a summary of the experimental method is presented here.

In the present experiments, ruby crystals were shocked along the crystal a axis, a pure mode direction.[15] The crystals were cut from oriented cylindrical rods from a large boule grown by Union Carbide. The chromium concentration of the a-cut ruby was approximately 0.4% Cr_2O_3 by weight, and the crystal orientation was known to within $\pm2°$. Two types of experiments were conducted in the present work: (a) uniaxial-strain compression of the ruby followed by partial unloading; these experiments utilized ruby disks that were 19 mm in diameter and 0.25

mm thick; and (b) uniaxial-strain compression of ruby followed by uniaxial-strain tension through wave interactions; these experiments utilized ruby disks that were 19 mm in diameter and 3.175 mm thick. The compression experiments were conducted at room temperature, and the tension experiments were conducted at 77 K. As indicated in the next section, the temperature differences had no bearing on the wavelength shifts, but the spectra quality was better at 77 K.

Plane shock waves were generated by impacting the samples with *z*-cut sapphire plates mounted on projectiles and accelerated to desired velocities using a single-stage light gas gun.[16,17] The impact velocities ranged between 200 and 600 m/s, yielding longitudinal stresses ranging between +125 kbar (compression) and −105 kbar (tension). As discussed in the next section, these values are well within the elastic response of sapphire.[18] Details regarding sample alignment, impact tilt, and projectile velocity measurements are typical of plate-impact experiments and can be seen elsewhere.[16,17]

The overall experimental arrangement is shown in Fig. 1. The ruby luminescence was generated by exposing the target, consisting in part of an *a*-cut ruby sample, to 5145 Å laser light from a Coherent cw argon laser (Innova 90-6). The laser light was transmitted to the target using an optical fiber (Diaguide SMY400UV) 400 μm in diameter. Two aspheric lenses were employed to image the fiber output onto the ruby sample. The same fiber along with a dichroic beam splitter was used to collect and deliver the induced *R*-line luminescence to a double spectrograph (Spex 1680 with 1200-groove/mm gratings) for wavelength dispersion. The *R*-line spectrum was further dispersed over time using a Hadland streak camera (Imacon 790), and the streak image was subsequently intensified by a microchannel-plate image intensifier (ITT model F4113, P-11 phosphor) and recorded using an intensified vidicon detector (EG&G model 1254). The

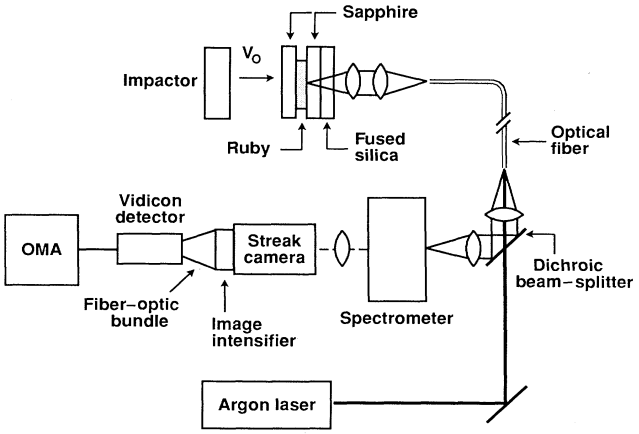

FIG. 1. Schematic view of the experimental arrangement; the thickness of the ruby has been exaggerated for clarity. Light from an argon laser is focused on to the ruby prior to impact through an optical fiber, and the induced *R*-line luminescence is collected by the same fiber. After spectral and temporal dispersion, the signal is recorded using an optical multichannel analyzer (OMA).

coupling between the image intensifier and the vidicon detector was accomplished by a tapered fiber-optic bundle (Galieo Electro-Optics, 3:1 reduction) which provided a high throughput. This arrangement yielded a spectral window of approximately 120 Å and a spectral resolution of 0.4 Å/channel. The time-resolved *R*-line spectra were recorded sequentially at 30-ns intervals for a total duration of 1.5 μs.

Figure 1 also shows the sample assembly used for the room-temperature compression experiments. It consisted of a thin ruby disk, two *z*-cut sapphire disks, and a fused-silica disk. The ruby and sapphire samples were obtained from Union Carbide, while the fused-silica disks (Dynasil 1000) were supplied by Adolph Meller. The sapphire and fused-silica disks were 25.4 mm in diameter, and their thicknesses varied from experiment to experiment. The ruby was placed between the two sapphire disks; the rear sapphire was backed by the fused silica. The four components were first glued together and subsequently potted into an aluminum target ring with epoxy. The sample configuration shown in Fig. 1 provided two data points corresponding to peak compression and partial unloading from the sapphire–fused-silica interface.

The sample assembly used for the 77-K tension experiments consisted of only two parts: a *z*-cut sapphire disk (31.73 mm diameter ×3.175 mm thick) backed by an *a*-cut ruby 19 mm in diameter and 3.175 mm thick. After being glued together, as discussed before, these two pieces were pressed against an aluminum cooling block to form a liquid-nitrogen cell with the aid of indium o-rings. The temperature of 77 K, measured by a *K*-type (Chromel-Alumel) thermocouple, was achieved by slowly pouring liquid nitrogen into the cell until it reached equilibrium. Tension in the ruby is produced through the interaction of rarefaction waves originating from the back of the sapphire impactor and the ruby. As described in Ref. 10, the impactor thickness is chosen to be half the ruby thickness to ensure that tension originates in the middle of the ruby.

Further details regarding experimental techniques including wavelength calibration may be seen in Refs. 8–10. Specific techniques related to low-temperature experiments are described in Ref. 8. A detailed discussion of the tension experiments including wave interactions is presented in Ref. 10.

Despite the use of *z*-cut sapphire and *a*-cut ruby in the sample assemblies, wave reflections do not arise in the present experiments. This is because of the following two factors: (a) For the low-chromium-concentration ruby used in the past and present work, the mechanical response of ruby and sapphire is indistinguishable,[19] and (b) the stress–particle-velocity relations for *z*- and *a*-cut sapphire are within ±0.4%.[18–20] Hence, as far as shock-wave propagation is concerned, the *z*-cut sapphire and *a*-cut sapphire or ruby are identical within experimental uncertainties. This issue is discussed further in Sec. V.

IV. RESULTS

A typical intensity-wavelength-time plot of the *R*-line spectra from a compression and tension experiment is

shown in Fig. 2. The data obtained are from an experiment with an impact velocity of 0.379 km/s, which resulted in a longitudinal stress of 85.9 kbar in compression and 82.5 kbar in tension. The procedure for obtaining the tensile-stress values is described in Ref. 10 and summarized later in this section. Because thick ruby samples were used in tension experiments, the transit time ($\sim$285 ns) of the shock wave in the sample is considerably larger than the experimental time resolution ($\sim$30 ns). Hence, after shock arrival in the ruby sample, two sets of R lines are observed in each spectrum in Fig. 2. These correspond to different combinations of ambient, compression, release, and tension states.[10] Except for specific tracks, the sample is subjected to two different stress states as discussed in Ref. 10. The intensity ratio for a particular track reflected the fraction of the sample that underwent compression or tension. Careful examination of the plot in Fig. 2 shows that upon unloading both R lines shift back to their ambient positions. This behavior, also observed for z-cut ruby,[10] is expected for elastic deformation. Two spectra that showed nearly pure compression and tension loading were selected from Fig. 2 (spectra 17 and 29) and are shown in Fig. 3 along with an ambient spectrum for comparison. Several interesting results can be seen readily from this figure: Both R lines exhibit a redshift in compression and a blueshift in tension, the separation of the two lines increases in both compression and tension, and there is no apparent broadening of the lines. Many of these results are in qualitative agreement with the c-axis results.[10] The one important difference is that along the a axis the R_1-R_2 separation increases for both compression and tension; for the c axis, the separation decreased under compression.

We have performed two compression (room temperature) and four tension (77 K) experiments resulting in a total of eight compression and four tension data points. The longitudinal stresses ranged from -105 to $+125$ kbar. The peak positions of the R lines in each track were determined by fitting the spectrum to either two Lorentzian or two Gaussian curves. We found that the Lorentzian model was more suitable for the room-temperature spectrum, while the Gaussian model provided a better fit to the low-temperature spectrum. In the compression experiments, the wavelength shifts of the R lines were obtained by averaging over the tracks corresponding to a particular stress value. In the tension experiment, however, only those spectra which yielded pure compression or tension loading were selected and averaged. Data from all six experiments were of good quality. As expected, the 77-K data were sharper and of a higher quality.

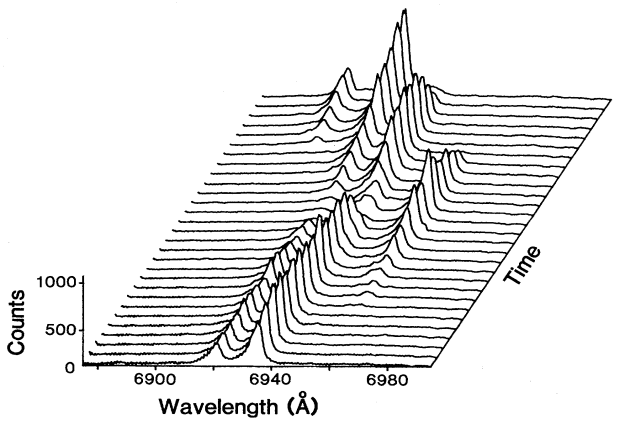

FIG. 2. Intensity-wavelength-time plot of the ruby R-line spectra obtained in a 83-kbar tension experiment at 77 K. The shock wave arrives at approximately track 8 where weak redshifted R lines are evident.

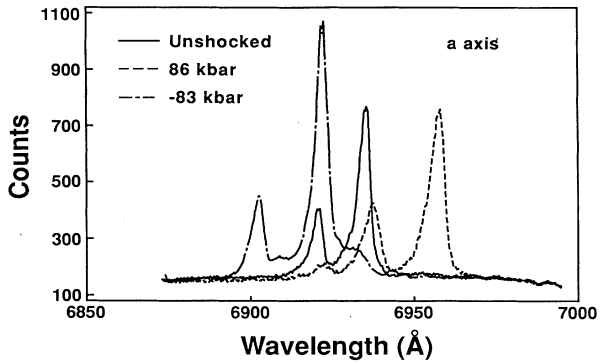

FIG. 3. Ruby R-line spectra at -82.5 kbar (long-short-dashed line), $+85.9$ kbar (dashed line), and ambient pressure (solid line), all of which were measured at 77 K.

The pertinent experimental parameters and the results from all six experiments are summarized in Table I; the format used is similar to that used in earlier studies.[9,10] Because of symmetric impact (sapphire on sapphire), the initial particle velocity corresponding to the peak-compression state is merely half the projectile velocity. The particle velocities corresponding to partial release and tension were calculated[9,10] using the stress-particle velocity relations for sapphire[20] and fused silica[20,21] and appropriate wave interactions. The procedure for calculating stresses and densities have been discussed in Refs. 9 and 10. As before, the two sets of values for longitudinal compression stresses shown in Table I are obtained from the measured shock data for sapphire[20] and the measured nonlinear elastic constants,[22] respectively. Excellent agreement is observed for these two sets of values.

The longitudinal stresses in tension and all lateral stresses were calculated using the nonlinear elastic constants as described earlier.[9,10] The tension calculations require some care as discussed in Ref. 10. Unlike the c-axis experiments, the two lateral stresses are no longer equal in the present case; for uniaxial strain along a axis, the c and m axes are not equivalent and lead to different lateral stresses.

The temperature rise was calculated as described in Ref. 9, and as expected, ΔT was very small for elastic compression. Although the temperature correction is within experimental precision, the room-temperature data were corrected to ensure consistency with previous work. The low-temperature data require no correction.[8]

We emphasize that stresses and densities of sapphire and fused silica, used in the present work, are known quite accurately. Good shock data exist for these materi-

TABLE I. Compilation of ruby a-axis data.

Experiment number[a]	Initial temperature (K)	Impact velocity (km/s)	Particle velocity[b] (km/s)	Density change	Longitudinal stress σ_{11}[c] (kbar)	Longitudinal stress σ_{11}[d] (kbar)	Lateral stress σ_{22} (kbar)	Lateral stress σ_{33} (kbar)	$\Delta\lambda_{R_1}$ measured (Å)	$\Delta\lambda_{R_2}$ measured (Å)	ΔT (K)	$\Delta\lambda_{R_1}$ corrected (Å)	$\Delta\lambda_{R_2}$ corrected (Å)
1			0.227	0.0203	103.4	103.3	35.1	24.2	26.8	20.6	7.7	26.4	20.2
(88 532)	300	0.454											
1_r			0.361	0.0083	41.9	41.9	14.0	9.5	10.2	8.0	3.2	10.0	7.8
2			0.275	0.0246	125.6	125.5	42.8	29.7	33.1	24.9	9.3	32.6	24.3
(88 541)	300	0.550											
2_r			0.438	0.0100	50.4	50.3	16.8	11.5	12.2	9.9	3.8	12.0	9.7
3			0.156	0.0139	70.5	70.4	23.7	16.3	17.9	14.5	1.4	17.9	14.5
(89 503)	77	0.312											
3_t			0.156	−0.0140		−68.1	−22.0	−14.7	−11.5	−14.9	1.4	−11.5	−14.9
4			0.190	0.0169	86.0	85.9	29.0	20.0	22.0	16.0	1.5	22.0	16.0
(89 504)	77	0.379											
4_t			0.190	−0.0171		−82.5	−26.5	−17.6	−13.2	−18.1	1.5	−13.2	−18.1
5			0.049	0.0044	21.9	21.8	7.2	4.9	5.3	4.3	0.4	5.3	4.3
(89 510)	77	0.098											
5_t			0.049	−0.0044		−21.6	−7.1	−4.8	−3.8	−3.8	0.4	−3.8	−3.8
6			0.243	0.0217	110.7	110.6	37.6	26.0	29.1	21.6	2.2	29.1	21.6
(89 511)	77	0.486											
6_t			0.243	−0.0219		−104.9	−33.5	−22.2	−15.5	−24.2	2.2	−15.5	−24.2

[a]Subscripts r and t denote partial release and tension data, respectively.
[b]The release data are calculated using the results of Barker and Hollenbach (Ref. 20) on z-cut sapphire and fused silica.
[c]Calculated using the data of Barker and Hollenbach on z-cut sapphire, except the tension data which were calculated using the nonlinear elastic constants obtained by Hankley and Schuele (Ref. 22).
[d]Calculated using the nonlinear elastic constants given by Hankley and Schuele.

als, and the excellent agreement between the shock results and nonlinear elastic calculations provides a good check.[9] Hence the largest uncertainty in the present work arises in measuring the wavelength shift and this is estimated to be ±0.5 Å.

In Fig. 4 the wavelength shifts of both R lines from all six experiments (compression and tension) are plotted as a function of density change ($\mu=\rho/\rho_0-1$). The solid lines in Fig. 4 are the quadratic fits $\Delta\lambda=a\mu+b\mu^2$ to the measurements. The compression and tension data were fitted separately because of the asymmetric response of the R lines for uniaxial strain along the a axis; the parameters a and b used to fit the data are listed in Table II. The maximum uncertainty in the coefficients is estimated to be 16%, except for $b=-8558$ Å, which is uncertain by approximately 30%. For the purpose of comparing with the theoretical work,[11] we also fitted the mean of the R_1 and R_2 line shifts (in cm^{-1}) to a quadratic expression, and the results are also listed in Table II.

In addition to the asymmetry, the R_1 line shifts faster toward the red (longer wavelength) in compression but slower toward the blue in tension as compared to the R_2 line. This implies, in conjunction with the relative energies of the two R lines, that the separation of the two R lines increases in both compression and tension, in contrast to the c-axis results[10] as noted earlier. Furthermore, the dependence of the R_2-line shift on uniaxial strain along the a axis, although not symmetric with respect to

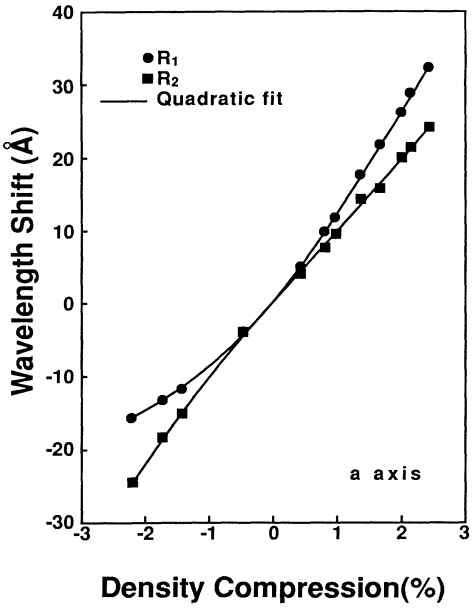

FIG. 4. Wavelength shifts of the R_1 and R_2 lines as a function of density compression along the crystal a axis. The solid lines are the quadratic fits to the experimental data. The uncertainty of each datum is represented by the size of the symbol used here.

TABLE II. Coefficients for quadratic fits to R-line shifts.

Coefficient	R_1-line shift (Å) Compression	Tension	R_2-line shift (Å) Compression	Tension	Mean shift (cm^{-1})
a	1163	981	987	920	-2163.8 ± 12.2
b	7160	12 400	0	-8558	$-11\,453\pm993$

the ambient density, is linear in compression. The uncertainty in each measured value (approximately 0.5 Å) in Fig. 4 is represented by the size of the symbols used in the plot.

V. ANALYSIS AND DISCUSSION

In this section we compare our a-axis results to the earlier c-axis shock data[9,10] and hydrostatic data.[2] The effect of crystal orientation on the R-line shifts is discussed using the theoretical developments presented in Ref. 11 and extended in Sec. II. The optical results are also compared with continuum observations in shocked sapphire. We shall focus our discussion on three important aspects of the data: R_1-line shift, R_2-line shift, and R_1-R_2 separation. Parts of Figs. 5 and 6 to be discussed in this section have been presented in Ref. 12.

A. R_1-line shift

In Fig. 5 we plot the R_1-line shift as a function of density change for both compression and tension along the c and a axes, together with the hydrostatic measurements (i.e., 0.366 Å/kbar). The pressure-density relation used for plotting the hydrostatic results was obtained using a Murnaghan equation with a bulk modulus of 2.544 Mbar (Ref. 23) and a pressure derivative of the bulk modulus as 4.275.[23] Because no hydrostatic data exist for tension, we extrapolated the hydrostatic measurements into tension for the purpose of comparing with shock-wave results.

It can be readily seen from Fig. 5 that the response of

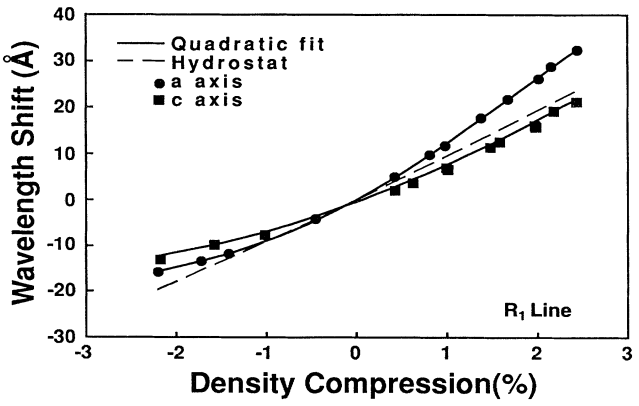

FIG. 5. Wavelength shifts of the R_1 line as a function of density compression along the crystal a and c axes. The dashed line is a fit to the hydrostatic data and is extrapolated into tension for purposes of comparing with shock-wave tension data.

the R_1 line to uniaxial strain is anisotropic. Under both compression and tension, the shift for strain along the a axis is larger than the shift for strain along the c axis for a comparable density change. In comparing with the hydrostatic results, the a-axis results show larger shifts under compression than the hydrostatic data, but the c-axis results show smaller shifts. However, under tension both a- and c-axis results show smaller shifts in comparison with the extrapolated hydrostatic curve.

The experimental results indicated above can be analyzed and understood using the theoretical model presented by Sharma and Gupta[11] and extended here in Sec. II. By expressing a given deformation or strain in terms of the irreducible strain representations,[11] the parameters defined in Sec. II can be used to evaluate and understand the contributions due to each of the irreducible strains. The discussion in this and the next subsection follows closely the arguments and findings presented in Sec. VI of Ref. 11.

For a given density compression, the contribution of $e(A_1)$ to the mean shift is identical for both a and c axes, resulting in a redshift of the mean in compression and a blueshift in tension. However, the contributions from trigonal and other strain components vary with loading conditions[11] and are responsible for the differences in Fig. 5. Compression along the c axis reduces the trigonal field [i.e., $e_{x_0}>0$], resulting in a blueshift of the mean followed by a decrease in splitting [Eq. (10)]. For the lower-energy R_1 line, this decrease in splitting gives rise to an additional blueshift. Because the magnitude of the overall shift of the R_1 line is determined by contributions from both $e(A_1)$ and $e_{x_0}(T_2)$, the net shift of the R_1 line for strain along the c axis will be smaller in comparison with hydrostatic data which only have the $e(A_1)$ contribution. This is indeed observed in Fig. 5.

In contrast to the c axis, compression along the a axis increases the trigonal field [i.e., $e_{x_0}<0$], giving rise to a redshift of the mean. In addition, Eq. (12) shows that the R_1-R_2 splitting increases for both compression and tension. For the lower-energy R_1 line, this corresponds to an additional redshift. Thus the overall redshift of the R_1 line for compression along the a axis is larger than the hydrostatic data, which only have the $e(A_1)$ contribution.

Under tension, R_1-R_2 splitting increases for both c and a axes and introduces a small redshift of the R_1 line as discussed above. Along the a axis, the trigonal strain increases in tension, resulting in a blueshift of the mean. Along the c axis, however, the trigonal strain decreases, giving rise to a redshift of the mean. The magnitude of the blueshift due to the decrease of the trigonal field for

strain along the a axis turns out to be smaller than the redshift caused by the change in splitting. Thus the overall blueshift under tension for strain along a axis is less than the hydrostatic extrapolation. For strain along the c axis, the additional redshift due to the decrease of the trigonal strain further reduces the overall blueshift. This explains the smaller blueshift observed in tension in comparison with the a-axis data and the hydrostatic extrapolation.

B. R_2-line shift

Unlike the R_1 line, the measured shift of the R_2 line, shown in Fig. 6, does not display any dependence on crystal orientation under compression. In fact, the results along both orientations agree very well with the hydrostatic measurements over the entire compression range examined (up to 2.5% density compression). However, under tension the shift of the R_2 line depends on crystal orientation as shown in Fig. 6.

This isotropic behavior of the R_2 line under compression can again be explained using the arguments presented in Ref. 11. The isotropy arises from the balance between the mean shift from trigonal and rhombic distortions [$\Pi(e_{x_0})$ and the quadratic term for the mean discussed in Sec. II] and the change in splitting [Eqs. (10) and (12)].

Along the c axis, the uniaxial-strain compression gives rise to a decrease in trigonal field [i.e., $e_{x_0}>0$]. The net contribution from $\Pi(e_{x_0})$ and the quadratic term is thus a blueshift of the mean. This decrease in the trigonal field also results in a decrease of the line splitting and, hence, a redshift of the higher-energy R_2 line. These two strain effects tend to cancel, and as a result, the overall change of the R_2 line is a redshift due to uniform compression [i.e., $e(A_1)$] as in hydrostatic loading.

For a-axis compression, the increase in splitting given by Eq. (12) arises due to tetragonal distortion. For the higher-energy R_2 line, this increase corresponds to a blueshift, but the trigonal strain now has a different sign, leading to a redshift of the mean. Again, these two terms cancel and only the uniform strain contributes to the overall redshift of the R_2 line as in the hydrostatic case. Our measurements show that the magnitudes of these two effects are approximately equal over the entire compression range (up to 125 kbar) along the a or c axis.

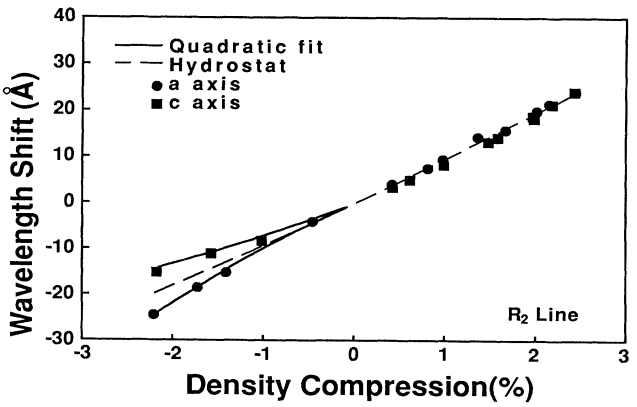

FIG. 6. Wavelength shifts of the R_2 line as a function of density compression along the crystal a and c axes. The dashed line represents the hydrostatic measurements and is extrapolated to tension for purposes of comparing with shock-wave tension data.

Under tension, the increase in the R_1-R_2 splitting gives rise to a small blueshift of the R_2 line for strain along either the c or a axis in addition to the blueshift from uniform strain [$e(A_1)<0$]. However, the trigonal strain decreases for tension along the c axis and increases for tension along the a axis, the former introducing a small redshift to the mean, while the latter introducing a small blueshift to the mean. As a result, the magnitude of the overall blueshift of the R_2 line is reduced for tension along the c-axis in contrast to the a-axis data as shown in Fig. 6.

In tension, the deviation of the c-axis data from the hydrostatic extrapolation is due to the contribution from the quadratic term discussed in Sec. II. This term reduces slightly the blueshift due to trigonal strain in compression, but increases the redshift in tension. Because this mean shift and the shift due to change in splitting cancel in compression, these two effects will not cancel in tension and there exists a residual redshift which reduces slightly the overall blueshift. As a result, the R_2-line shift for tension along the c axis is smaller in comparison to the hydrostatic extrapolation.

The deviation of the a-axis curve from hydrostatic extrapolation in tension can be readily understood since both trigonal contribution to the mean and R-line separation give rise to a blueshift in tension (recall $e_{x_0}>0$ and R_1-R_2 increases in tension) in addition to the blueshift due to uniform strain. Thus the overall shift for the strain along the a axis is expected to be larger than the hydrostatic extrapolation, as shown in Fig. 6.

C. R_1-R_2 separation

In Fig. 7 we plot the change in R_1-R_2 splitting as a function of density change for both c- and a-axis deformation (note that the unit for shift is now in cm^{-1}). Several interesting results can be readily seen from this figure, which represents perhaps the most interesting findings of the present work. The magnitude of the change in splitting for strain along the a axis is strongly nonlinear and up to a factor of 4 larger in comparison to the c-axis data. The R_1-R_2 splitting increases for both compression and tension in the a-axis data as predicted by the theoretical model. Furthermore, the a-axis curve is not symmetric with respect to a change in the sign of the density compression. In contrast, the R_1-R_2 splitting in the c-axis data varies linearly with density compression and is larger in tension. These results demonstrate clearly the anisotropy in the optical measurements.

Our extension of the theoretical work by Sharma and Gupta[11] is particularly helpful in analyzing the data presented in Fig. 7. The earlier analysis, neglecting the higher-order contributions, concentrated on the slopes in the vicinity of the origin. Here we analyze the data over

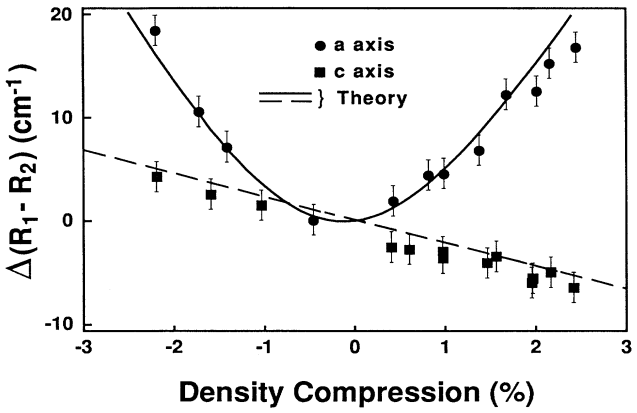

FIG. 7. Change in the R_1-R_2 splitting as a function of density change along both the a and c axes. The solid and dashed lines are theoretical predictions obtained using Eqs. (10) and (12).

the entire range shown in Fig. 7.

According to Eq. (12), the large change in splitting along the a axis is due to the presence of the tetragonal distortion represented by q. Further analysis shows that the rhombic and tetragonal contributions have opposite signs, and because of this, the splitting change due to q is reduced by almost a factor of 2. The slight asymmetry of the a-axis curve around the origin stems from the first term in Eq. (12) [i.e., trigonal distortion], which decreases in tension and increases in compression.[11] Thus it pulls the left side of the curve down and pushes the right side up slightly. For small tensions (less than -0.5% density compression), the first term dominates the overall change in splitting, giving rise to a slight decrease of the R_1-R_2 separation.

As discussed in Sec. II, the value of q which is a measure of the tetragonal contribution to the R_1-R_2 splitting can be determined from the shock-wave results along the a axis. Recall that K_1 in Eq. (12) has been independently obtained from the c-axis data. To evaluate q, we fitted Eq. (12) to the measured change in R_1-R_2 splitting (solid line in Fig. 7) and found q to be approximately 3183.8 cm^{-1}. We emphasize that the fit shown in Fig. 7 was not optimized. We simply chose a value that yielded a reasonable fit to the measured change in both compression and tension; the agreement between theory and experiment is very good. The value of q obtained here is 1.24 times the value obtained in Ref. 11. This difference can be attributed to the approximation employed in Ref. 11 in calculating the line splitting for the a-axis data at low compressions. The dashed line in Fig. 7 is the theoretical prediction for the change in R_1-R_2 splitting for the c-axis data [Eq. (10) with $K_1 = -3459.5\ \mathrm{cm}^{-1}$].

Further analysis shows that for uniaxial-strain compression along the a axis, the contribution of the second term in Eq. (12) to the R_1-R_2 splitting is very small ($<0.4\%$) and can be neglected. The term in the square brackets dominates the splitting change at strains larger than $\pm 0.5\%$. The last term in the square brackets, $K_1^2 e^2/4A$, contributes approximately 2% of the change to splitting at a density compression of 2.5%.

An important finding from the data in Fig. 7 is a direct demonstration of the site or local symmetry changes in a shocked crystal. This result is in contrast to the continuum results discussed below.

D. Comparison with continuum measurements

An important objective of our work was to examine the use of R-line shifts to probe the microscopic changes around the Cr^{3+} ion in shocked sapphire. To put the present work in proper perspective, it is useful to first consider continuum measurements in shocked sapphire.[18,20] For the present discussion, we focus our attention only on the elastic response of shocked sapphire. Graham and Brooks[18] have shown that, below the elastic limit, the sapphire Hugoniot does not depend on the crystal orientation for the three orientations they examined. In addition, the response of shocked sapphire below the elastic limit is in excellent agreement with finite-strain calculations using nonlinear elastic constants.[9] To demonstrate the closeness in the mechanical behavior of sapphire shocked along the c and a axes, we plot, in Fig. 8, the difference in longitudinal stresses along the a axis (σ_{11}) and along the c axis (σ_{33}) as a function of particle velocity. Over the elastic range of sapphire, the σ-u response of c- and a-cut sapphire differs by less than 0.4% and confirms that the shock response of sapphire is isotropic. Recall that lateral stresses will be somewhat different in the two cases.

In contrast to the continuum results, the optical data shown in Fig. 7 demonstrate strong anisotropy which arises due to strain-induced local symmetry changes around the Cr^{3+} ion. The luminescence data are rich in detail and provide insight into microscopic changes that cannot be discerned from continuum measurements. Furthermore, the optical data can be used to separate contributions due to density compression, nonhydrostaticity, and crystal orientation. As demonstrated in the present work, the R_1-R_2 splitting provides an excellent

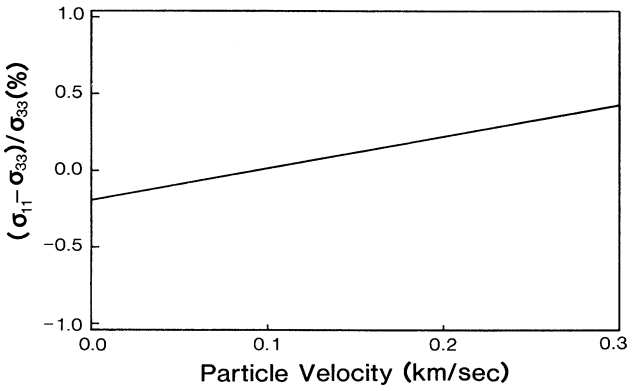

FIG. 8. Calculated difference in longitudinal stress along the c axis (σ_{33}) and a axis (σ_{11}) as a function of particle velocity using the nonlinear constants of Hankley and Schuele (Ref. 22). Over the entire elastic range (up to 2.5%), this difference is less than 0.4%.

measure of stress deviators in the crystals provided the crystal orientation is known. The ability to directly obtain this information is an important step in characterizing shocked solids.

By design, the focus of the present work was on the elastic response. In the elastic region, the various macroscopic parameters (density changes, stress components, etc.) are known and their relationship to the details in the optical spectra can be determined. In the inelastic region, where all the macroscopic parameters under shock loading are not established, the optical spectra can then be used to provide information about macroscopic parameters of interest. In addition, the changes in the local environment due to inelastic deformation can be probed using fluorescence from dopant ions. We are currently investigating the use of R lines to examine shock-induced inelastic deformation in sapphire.

E. Implications for DAC studies

Results of our R_1- and R_2-line shifts under compression have interesting implications for DAC measurements, and these have been presented in detail in Ref. 12. Here we simply reiterate that the use of oriented ruby chips is desirable for pressure measurements in a nonhydrostatic environment. The present results show clearly that nonhydrostatic deformation by itself is not the cause of line broadening in ruby R-line emission. The stress gradients or nonuniform stresses are the cause of line broadening in DAC studies, and this effect can be examined quantitatively by using oriented ruby chips.

VI. CONCLUSIONS

The present work has provided a comprehensive understanding of crystal-orientation effects on ruby R-line shifts caused by elastic deformation. The rapid loading due to shock-induced deformation was incidental to the present work. The principal benefits of shock-wave loading were twofold: well-defined loading along a particular crystal orientation and the ability to produce strongly nonhydrostatic but uniform stresses. These experimental features were essential for separating the various contributions to R-line shifts in a quantitative manner.

The strong anisotropy observed in the optical data is in marked contrast to the isotropy observed in the continuum data. This finding points out the usefulness of using optical spectra as a microscopic probe of shocked materials. The nonlinear increase in R-line separation under both compression and tension (Fig. 7) provides direct evidence of site-symmetry changes around the Cr^{3+} ion.

The theoretical model developed by Sharma and Gupta[11] provides a basis for understanding ruby R-line shifts in a consistent manner under a broad range of loading conditions: shock-wave compression and tension, hydrostatic, and uniaxial-stress loading. In the present work, we have extended the previous theoretical developments[11] to permit analysis of the R-line shifts under arbitrary deformations. This generalization is important because we now have a method to analyze R-line shifts under any arbitrary deformation for any orientation in a quantitative manner. The main conceptual restriction, as before,[11] being that the strain-induced changes be represented by a perturbation Hamiltonian.

As discussed in an earlier paper,[12] the use of oriented ruby chips in DAC experiments would go a long way toward providing an accurate pressure calibration in DAC experiments under nonhydrostatic loading. The present data show that the a-axis orientation is particularly useful because nonhydrostaticity in the ruby causes increased R-line separation and makes it easier to determine the R_1- and R_2-line shifts. The principal difficulty in pressure calibration in a nonhydrostatic medium at larger compressions in DAC experiments is due to the combination of stress gradients and the lack of knowledge regarding ruby orientation. Use of oriented chips (e.g., a-axis ruby) can permit an evaluation of these gradients using the developments presented in our work.

A final test of our theoretical work involves prediction of R-line shifts along an arbitrary crystal orientation. This task and extension of our work to examine shock-induced inelastic deformation at a microscopic level are subjects of ongoing work and will be presented in the future.

ACKNOWLEDGMENTS

The present work has built on the earlier experimental work of Paul Horn and Jim Burt, and discussions with these individuals were very beneficial to us. We particularly want to express our sincere appreciation to Surinder Sharma whose pioneering work on the theoretical aspects of the ruby problem were essential to the developments presented here. His comments on the present manuscript were most helpful. J. K. Hyun is thanked for carefully going through the derivations and pointing out some sign errors. Jerry Thompson and Paul Bellamy are thanked for their assistance in performing the shock-wave experiments. This work was supported by DNA under Contract No. 001-88-C-0070.

*Present address: SRI International, Menlo Park, CA 94025.

[1]G. J. Piermarini, S. Block, J. D. Barnett, and R. A. Forman, J. Appl. Phys. **46**, 2774 (1975).
[2]R. G. Munro, G. J. Piermarini, S. Block, and W. B. Holzapfel, J. Appl. Phys. **57**, 165 (1985).
[3]H. K. Mao, P. M. Bell, J. W. Shanner, and D. J. Stienberg, J. Appl. Phys. **49**, 3276 (1978).
[4]J. A. Xu, H. K. Mao, and P. M. Bell, Science **232**, 1404 (1986).
[5]A. Jayaraman, Rev. Mod. Phys. **55**, 65 (1983).
[6]J. H. Egert, K. A. Goettel, and I. F. Silvera, Phys. Rev. B **40**, 5724 (1989).
[7]P. D. Horn and Y. M. Gupta, Appl. Phys. Lett. **49**, 856 (1986).
[8]J. A. Burt, Ph.D. thesis, Washington State University, 1989.
[9]P. D. Horn and Y. M. Gupta, Phys. Rev. **39**, 973 (1989).
[10]Y. M. Gupta, P. D. Horn, and J. A. Burt (unpublished).
[11]S. M. Sharma and Y. M. Gupta, Phys. Rev. B **43**, 879 (1991); **48**, 3579(E) (1993).
[12]Y. M. Gupta and X. A. Shen, Appl. Phys. Lett. **58**, 583 (1991).

[13]S. Sugano, Y. Tanabe, and H. Kamimura, *Multiplets of Transition Metal Ions in Crystal* (Academic, New York, 1970).

[14]In the case of uniaxial-strain compression along the c axis, i.e., $e_{x_0}=e/\sqrt{3}$ and $|e_{x_-}|=0$, the quadratic contribution to the mean is proportional to $2K_1^2e^2$. For uniaxial strain along the a axis, however, we have $e_{x_0}^2=|e_{x_-}|^2=e^2/12$ and the corresponding term now becomes $\frac{3}{2}K_1^2e^2$. The curvature ratio for the a- and c-axis shifts is thus $\frac{3}{4}$. The observed curvature along the c axis is $-16\,339.4$ [Eq. (3) in Ref. 11], which suggests the curvature for a-axis compression to be approximately $-12\,254.6$ in good agreement with $-11\,453\pm933$ measured along the a axis (see Table II in the text).

[15]S. F. S. Hearmon, *An Introduction to Applied Anisotropic Elasticity* (Oxford University Press, London, 1961).

[16]G. R. Fowles, G. E. Duvall, J. Asay, P. Bellamy, F. Feistman, D. Grady, T. Michaels, and R. Mitchell, Rev. Sci. Instrum. **41**, 984 (1970).

[17]Y. M. Gupta, D. D. Keough, D. F. Walter, K. C. Dao, D. Henley, and A. Urweider, Rev. Sci. Instrum. **51**, 183 (1980).

[18]R. A. Graham and W. P. Brooks, J. Phys. Chem. Solids **32**, 2311 (1971).

[19]T. Kottke and F. Williams, J. Appl. Phys. **54**, 6749 (1983); the results in this paper, along with the other results cited, agree with the results based on the elastic constants cited in G. Simmons and H. Wang, *Single Crystal Elastic Constants and Calculated Aggregate Properties: A Handbook* (MIT, Cambridge, MA, 1971).

[20]L. M. Barker and R. E. Hollenbach, J. Appl. Phys. **41**, 4208 (1970).

[21]M. P. Conner, M.S. thesis, Washington State University, 1988.

[22]R. E. Hankley and D. E. Schuele, J. Acoust. Soc. Am. **48**, 190 (1970).

[23]H. d'Amour, D. Schiferl, W. Denner, H. Schulz, and W. B. Holzapfel, J. Appl. Phys. **49**, 4411 (1978).